Chemotactic behavior of *Escherichia coli* at high cell density

Remy Colin*
Victor Sourjik*
Max Planck Institute for Terrestrial Microbiology
Loewe Center for Synthetic Microbiology
Karl-von-Frisch-strasse 16, 35043 Marburg, Germany

August 28, 2018

Abstract

Dense suspensions of swimming bacteria are known to exhibit self-organized collective motility patterns, observed both in artificial and natural situations, e.g. during swarming, pellicle biofilm formation or in travelling chemotactic bands. Coincidentally, bacteria must perform physiologically relevant functions, such as chemotaxis, which allows finding optimal ecological niches by biasing their otherwise random walk according to gradients of environmental conditions. Here we studied the influence of collective behavior on chemotaxis of the model organism *Escherichia coli* in attractant gradients created in microchannels, and varying cell density, cell length and the degree of two-dimensional confinement of bacterial suspension. The typical eddy size of swirling collective motion observed at high cell density was set by the channel height, while its magnitude scaled with cell volume fraction and swimming speed but also depended on the channel height. This indicated that the collective motion predominantly emerged as a result of hydrodynamic interactions between swimming bacteria. After reaching a maximum at an intermediate volume fraction of about 1 %, chemotaxis was strongly impaired by the collective motion, with the chemotactic drift decreasing exponentially with its magnitude. At moderate confinement, elongated cells retained their chemotactic ability until higher density than normally-sized cells. Simulations of self-propelled, chemotactic and sterically-interacting rods were in qualitative agreement with the experiments, suggesting that reorientations induced by the physical interactions between cells were responsible for chemotaxis impairment. Collective motion thus exerts a strong physical control on the ability of bacteria to navigate chemical gradients, with important implications for high-density behaviors of motile bacteria.

Introduction

When the cell density of a suspension of swimming bacteria increases, collective motion emerges, characterized by intermittent jets and swirls of packs of cells [1–3]. This behavior has been

*To whom correspondence should be addressed. E-mail: remy.colin@synmikro.mpi-marburg.mpg.de, victor.sourjik@synmikro.mpi-marburg.mpg.de

extensively studied experimentally [4–7] and theoretically [8–13], and it is known to emerge from alignment between the self-propelled particles [14]. Two alignment mechanisms have been proposed to account for bacterial collective motion, based either on steric interactions between the rod-like bacteria [15–17] or on the hydrodynamics of the flow they create [8, 10], of pusher symmetry [3, 18, 19]. However, the relative importance of these mechanisms has not been clearly established so far [20]. Collective motion of microorganisms is observed not only in artificial but also in natural situations, often at an interface, e.g. when bacteria swarm on a moist surface in the lab [21–24] or during infection [25], or at an air-water interface during formation of pellicular biofilms [1, 26].

Bacterial collective motion contrasts to behavior of individual motile cells in dilute suspension, when bacteria swim in a succession of relatively straight second-long runs and short reorientations (tumbles), resulting at long times in a random walk by which they explore their environment [27]. Bacteria can further navigate in environmental gradients by biasing this motion pattern, lengthening (resp. shortening) their runs when swimming toward attractive (resp. repulsive) environment [27]. The signaling pathway controlling this chemotactic behavior is well understood in *E. coli* [28, 29] and one of the best modeled signaling systems [30]. Bacteria monitor – via their chemoreceptors – the changes in environmental conditions and respond to them by modifying a phosphorylation signal transmitted to the flagellar motors to change the tumbling frequency accordingly [31, 32]. An adaptation module slowly resets the receptor sensitivity for further stimulations, via a negative feedback loop [33, 34]. In *E. coli*, attractant substances repress the phosphorylation signal, which results in less tumbles, repellents having the opposite effect. That effectively allows the cell to compare its current situation to the recent past while swimming along a given direction [29], with a memory timescale of a few seconds [35, 36]. Notably, the rotational Brownian motion of the cell body interferes with this mechanism of sensing by randomly changing the direction of swimming while temporal comparisons are performed [27, 28].

Although typically seen as a single-cell behavior, chemotaxis also drives collective behaviors based on chemical interactions, such as autoaggregation [37, 38], self-concentration in patches [39, 40] and travelling band formation [41, 42], where chemotactic response to self-generated gradients of chemoattractants lead to local cell density increases. However, very little is known about how the high-density physical interactions and the resulting collective motion influence the chemotactic navigation of bacteria [43, 44]: e.g., would chemotaxis be improved by alignments of convective flows with the gradient [12, 44] or compromised by random collisions between cells? This lack of knowledge is in part due to the technical difficulty of measuring the dynamics of cells in a dense sample [13]. Over the last few years, new image analysis methods have been developed or adapted to bacterial systems [2, 45–48], which exploit intensity fluctuations [45] or intensity pattern shifts [48] to characterize swimming and chemotaxis in populations of bacteria. These Fourier image analysis methods function at virtually arbitrary cell density, capture the dynamics of all cells non-selectively, and are at least as fast as more commonly used particle tracking.

In this paper, we used Fourier image analysis methods to investigate how the collective motion developing with increasing cell density affects the ability of *E. coli* population to follow controlled chemical gradients in a microdevice. Our experimental results and computer simulations showed that, after an initial increase, chemotaxis was reduced as collective motion developed in the sample. Collective reorientations acted similarly to an active rotational diffusion interfering with the chemosensing mechanism. Additionally, the characteristics of the

collective motion hinted at its hydrodynamic origin, with possible additional steric effects under increased two-dimensional confinement. These results have important implications for collective behaviors of motile bacteria at high density.

Results

Measuring chemotaxis at arbitrary cell density

Microfabricated devices made of the oxygen-permeable polymer poly-dimethylsiloxane (PDMS) were used as described previously [48] to create quasi-static linear gradients of the non-metabolizable attractant α-methyl-D,L-aspartic acid (MeAsp) in a straight channel (Fig. 1*A*). This gradient could be mimicked using the fluorescent dye fluorescein (Fig 1*B*), which has a diffusion coefficient similar to the one of MeAsp ($D \simeq 500\,\mu\text{m}^2/\text{s}$). Three channel heights, $h = 50$, 30 and $8\,\mu$m, were used to increasingly confine the cell suspensions towards two dimensions. Motility of suspensions of *E. coli* bacteria, measured in the middle of this gradient, was sustained for several hours at all cell densities (SI Fig. S1), due to oxygen availability and abounding energy source in the medium. When the density increased, the development of collective motion in the sample, characterized by the existence of collective eddies and jets of swimming cells was observed (Fig. 2*A*) as expected [2, 6, 13]. The shape of the gradient, after the transient phase during which it became established, was largely unaffected by the collective motion (Fig. 1*C*), except at the highest bacterial cell body volume fractions. Although steering by the bacteria might have affected the diffusion of MeAsp [49], the Peclet number, which compares diffusion and transport of MeAsp in an eddy, remained moderate ($Pe = hv_f/D \leq 1$, where v_f is the fluid velocity; see SI text). Furthermore, in the present geometry, at steady state the gradient shape does not depend on the diffusion coefficient. Because the cell density slowly changes with time in the area of measurement due to the chemotactic accumulation, thus differing from the average cell density in the suspension, the cell body volume fraction Φ_c was measured *in situ* in each experiment (SI Fig. S2 and *Materials and Methods*).

To further investigate the effect of cell elongation, which is typically observed for bacteria swarming on a wet hydrogel at high density [21], we compared normally-sized *E. coli* with average length $L = 2\,\mu$m and cells elongated to an average of $L = 4\,\mu$m upon treatment with cephalexin, a drug preventing cell division (*Materials and Methods* and SI Fig. S2). Because we observed that the cephalexin treatment strongly increased cell autoaggregation, which is mediated in this *E. coli* strain by the adhesin Antigen 43 [37], in subsequent experiments we used Δ*flu* strain deleted for the gene encoding this adhesin. In absence of the cephalexin treatment, *flu*+ and Δ*flu* cells behaved similarly, regarding both their collective motion and chemotaxis (SI Fig. S3), and the elongated Δ*flu* cells showed normal motility (SI Fig. S1).

Structure of the collective motion

The collective motion was measured using an image velocimetry method derived from Phase Differential Microscopy [48] (*Materials and Methods*) to quantify the local velocity field $\mathbf{v}(\mathbf{r})$, averaged over several neighboring bacteria (Fig. 2*A*). The spatial structure of the flow field at varying Φ_c was characterized by the 2-dimensional power spectral density of the velocity field

(*Materials and Methods*):

$$E(q) = q \left\langle \frac{\tilde{\mathbf{v}}(\mathbf{q},t)\tilde{\mathbf{v}}^*(\mathbf{q},t)}{A_0\langle v^2\rangle} \right\rangle_{t,|\mathbf{q}|=q} . \tag{1}$$

This quantity (Fig. 2*B*) measures the distribution of kinetic energy over the flow structure sizes π/q, hence representing the probability to observe a "vortex" of size π/q [13]. At $\Phi_c \gtrsim 1\%$, it exhibited, at a low wave number $q_{\max}$, a maximum $E(q_{\max})$, which grew as density increased (Fig. 2*B*). After an initial decrease, the value of $q_{\max}$ reached a plateau q_{str} at moderate cell density, corresponding to $E(q_{\max}) \gtrsim 15\,\mu$m (SI Fig. S4A). Fully developed collective motion thus takes the form of flow structures (eddies) with a specific size, π/q_{str}. An increase in cell density results in an increase of the amount of collective flow of this size – the amplitude of the collective motion, which can be quantified by $E(q_{\text{str}})$. Interestingly, q_{str} was apparently determined by the height h of the channel (Fig. 2*C* inset and SI Fig. S4*A*), indicating that the flow structures are constrained by the system size. The observed decrease of $q_{\max}$ at low cell density might be due to a combination of $E(q_{\max})$ reaching the noise level, represented by the featureless $E(q)$ observed at the lowest densities, and a genuine reduction of the eddy size when cell density becomes low.

For simplicity, the amplitude of the collective motion was quantified by $E(q_{\text{str}})$ at all volume fractions (Fig. 2*C* and SI Fig. S4*B,C*). We observed that $E(q_{\text{str}})$ tended to grow more slowly with volume fraction for more confined suspensions (lower h). At moderate confinement ($h = 30$ and $50\,\mu$m), $E(q_{\text{str}})$ also grew more slowly for longer cells, whereas for $h = 8\,\mu$m it was on the contrary a single function of Φ_c for both cell lengths (Fig. 2*C*). Importantly, when corrected for background noise and normalized to its value at high Φ_c, $E(q_{\text{str}})$ was found to be for all conditions a single function of $\Phi_c v_0\,\pi/q_{\text{str}}$, where v_0 is the population-averaged swimming speed of the cells (SI Fig. S4*D*). Notably, v_0 increased with Φ_c, and thus with $E(q_{\text{str}})$ (SI Fig. S1*B-C*).

Chemotaxis dependences on cell density

For non-interacting cells in 3D, v_0 and the chemotactic velocity v_{ch} in a chemical gradient are expected to be related as [50–52]:

$$v_{ch} = G v_0^2 \tau\left(\tau_m, \tau_0, D_r\right) \nabla f(c)\,, \tag{2}$$

where G is the total gain of the chemotaxis system, τ is a time depending on the steady state tumbling rate τ_0, the memory time scale τ_m and the rotational diffusion of the cell D_r, and $f(c)$ is a chemoreceptor free energy shift due to the binding of chemical ligand present at concentration c. In absence of interactions, v_{ch}/v_0^2 thus depends only on internal – fixed – parameters of the chemotaxis pathway and on the fixed concentration profile. This quantity was therefore used to quantify chemotactic efficiency.

The MeAsp gradient (from 0 to 200 μM in 2 mm) was chosen to maximize the chemotactic coefficient v_{ch}/v_0^2 at low density [48]. For all combinations of cell length and channel height, the chemotactic coefficient first tended to increase when the cell density Φ_c increased in the range $0.05 - 1\,\%$, before strongly decreasing above a condition-dependent Φ_c, corresponding to the density above which collective behaviors were observed (Fig. 3*A-C*). Collective motion thus apparently impaired the ability of the cells to perform chemotaxis.

Chemotaxis was also affected by cell length and channel height. Even at low cell density, $4\,\mu$m long cells, as well as less confined cells, had a higher chemotactic coefficient v_{ch}/v_0^2 (Fig. 3*A*). Cell

elongation is indeed expected to result in increased chemotactic drift in steady gradients [53], because of the lower rotational diffusion of longer cells [50] and their expected reduced tumbling angle [41, 54]. To directly compare the pure effect of cell density under various conditions, chemotactic coefficients were thus normalized to the average low density ($\Phi_c < 0.15\,\%$) value in each condition (Fig. 3*B,C*). Even this normalized chemotactic coefficient was significantly higher for longer cells at $\Phi_c > 1\%$ under moderate confinement (Fig. 3*B*). It was however a single function of Φ_c, irrespective of cell length, for $h = 8\,\mu$m (Fig. 3*C*). Chemotaxis also tended to be higher for a stronger confinement, all else being equal.

Collective motion controls chemotaxis

The behavior of the chemotactic coefficient was thus reminiscent of the one of $E(q_{\mathrm{str}})$. Indeed, the normalized chemotactic coefficient was found to be a single function of the amplitude of the collective motion $E(q_{\mathrm{str}})$, irrespective of the cell size and channel height (Fig. 3*D*), decreasing exponentially as a function of $E(q_{\mathrm{str}})$ from its low density value. The amplitude of the collective motion therefore appears to determine the reduction of the ability to sense gradients, irrespective of vortex size π/q_{str}, for $\Phi_c \gtrsim 1\,\%$, in all conditions.

As the indirect effect of gradient distortion by the swimming bacteria could be ruled out (Fig. 1), we hypothesized that the observed reduction of chemotaxis at high density was due to the forced reorientations resulting from the cell-cell interactions, which would interfere with the sensing mechanism by temporal comparisons: As the cell is swimming, it monitors the change in chemoattractant concentration within a few seconds, to decide whether to tumble. If during this time the direction in which the cell swims has changed significantly, the decision becomes less relevant thus making bacterial chemotaxis strategy inefficient. Collective reorientations then would act analogous to an enhancement of rotational diffusion – the time scale of sensing τ decreases as D_r increases [51, 52, 55], reducing the chemotactic coefficient accordingly (Eq. 2).

Simulations of cell-density effects on chemotaxis

To test whether collective reorientations may indeed reduce chemotactic drift, we performed numerical simulations of a population of self-propelled chemotactic rods of variable aspect ratio L, which interact via soft steric repulsion (Fig. 4*A* inset) and are confined in two dimensions in a viscous medium. Rods reorient rotationally when tumbling, with the tumbling probability being determined according to the concentration of chemoattractant experienced by the rod, using a model of the chemotaxis system of *E. coli* [56].

When the cell area fraction increased, the simulated rods formed increasingly large swirling packs of cells (Fig. 4*A*), similarly to previous reports [16, 17]. Notably, the typical time for which a rod persists swimming in a given direction was observed to decrease as the cell density increased (SI Fig. S5*A*-*B*) – reflecting increased collective reorientations because of increased collision rates. This decrease was slower for more elongated cells, similarly to the experimental observations, despite the mechanisms of reorientation in simulations and experiments likely being different (see Discussion).

The normalized chemotactic drift, plotted as a function of cell body area fraction, showed a general decrease (Fig. 4*B*), which was monotonous for $L = 2$ but had an additional peak for higher aspect ratios, similarly to what was observed in experiments (Fig. 3). Longer cells were also better at keeping track of the gradient for all densities. Already for area fractions as

small as 0.005, the chemotactic drift was significantly smaller than the one obtained in absence of steric interactions ($v_{ch}/v_0^2 = 1.51\,10^{-2}$ s/μm). Overall, the persistence time predicted well the chemotactic drift, irrespective of the aspect ratio (SI Fig. S5C). Further analysis showed that two co-occurring effects explain the chemotactic drift reduction (SI text). First, the mean chemoreceptor free energy shift (CFES), predicted to govern the chemotactic drift in absence of interactions [57], was reduced in proportions similar to the drift (SI Fig. S5D). This reduction of CFES was apparently due to the lower persistence of swimming (SI Fig. S5E), and it accounted for a large part of the drift reduction (SI Fig. S5F). However, even once this first effect was corrected for, collective reorientations appeared to also reduce the drift in a CFES-independent way (SI Fig. S5G).

Discussion

Although the principles of chemotactic sensing are fairly well understood for a single cell [28, 30], little is known of the effects of physical interactions between cells on chemotaxis, despite their frequent occurrence during self-concentration processes [37–42] or high-density collective motility [21, 22, 26]. Here we used a model system, a suspension of *E. coli* in a controlled environment, to investigate the effect of collective motion, emerging when cell density increases, on chemotactic sensing.

We extended the range of conditions for which the characteristics of the collective motion are measured, compared to previous works [2, 4, 6, 13, 16, 24]. We demonstrated the existence of bacterial flow structures, the size of which is set by the smallest system size, independently of cell length and volume fraction, in fully developed collective motion. An increasing amount of the kinetic energy of the system gets poured in this flow structure as the cell density increases. The amplitude of the collective motion was function of the product $\Phi_c v_0\, \pi/q_{\rm str}$, which represents the flux of bacterial mass integrated over the vortex size. These properties would suggest a hydrodynamic origin of the collective motion, at least in less confined situations, since the largest possible flow structure – set by system size – is predicted to dominate in hydrodynamics based collective motion [8]. Simulations also showed a reduction of the total kinetic energy under confinement at fixed Φ_c [58], similar to our experiments. Under stronger confinement ($h = 8\,\mu$m), the selected eddy size, although fixed, differed from the channel height. This suggests that under confinement smaller than cell size (flagella included) the mechanism is modified, with possible role of steric effects or of increasingly two-dimensional flow patterns.

Physical interactions between cells resulted in a strong reduction of the ability of *E. coli* to track chemical gradients, after an initial slight increase at low densities. The collective motion was the driver of this decrease, with its amplitude $E(q_{\rm str})$ being the sole determinant of reduced chemotactic bias for several different experimental conditions. An interesting possible consequence of this phenomenon is a physical mechanism for density regulation near sources of chemoattractants (e.g., nutrients), because the increased cell density around the source [59] would limit self-concentration by mechanically reducing chemotaxis. Notably, this could explain an early observation that the density of cells entering a capillary filled with chemoattractant saturates as a function of the cell density in the suspension [60]. Based on our results, the cell density for which the chemotactic drift is maximal, $\Phi_c \simeq 1\%$, is also expected to play a cutoff role, and is indeed the typical maximal cell density reached within travelling chemotactic bands [41, 42].

Chemotaxis reduction appears to be induced by an increased reorientation rate of cell bodies within the collective motion, since the gradient held well. This conclusion could be qualitatively supported by simulations. Although our simulations neglected long-range hydrodynamic interactions, collective motion of rods emerging from either short (steric) or long (hydrodynamics) range interactions share many features [15, 20], including such collective reorientations. In simulations, two effects of reorientations accounted for the changes in chemotactic drift as a function of cell density: First, they reduce the response of the signaling pathway, CFES, by shortening the time traveled up the gradient. This effect is similar to increased passive rotational diffusion [57], and it could therefore be interpreted as collisions increasing the effective rotational diffusion of the cells. Second, collective motion also decreases chemotactic drift directly. This is likely to be an out-of-equilibrium effect, because currents created by collective motion break detailed balance, a vital assumption of [57] (see SI text).

Whereas this second contribution always increased with volume fraction, the rotational-diffusion-like effect was non-monotonous for $L = 3$ and 4, which explained the peak of v_{ch}. The reduction of effective rotational diffusion inducing the peak could come from a partial stabilization of the directions of motion through multibody interactions. Supporting this, the persistence time stagnated as a function of cell area fraction in the conditions where a peak was observed. The chemotactic bias peaking at $\Phi_c \sim 1\%$ in experiments might have a similar origin, since chemoattractant gradients might favor the emergence of collective motility modes oriented in their direction via hydrodynamic interactions [12]. At low cell densities, this effect might reinforce swimming persistence along the gradients and thus enhance the drift, before its strong decrease upon the development of swirls at higher cell densities.

The strong reduction in chemotactic drift at cell densities typical of swarming ($\Phi_c \sim 30\%$) [22] suggests that, without specific counteracting mechanisms, chemotactic navigation within a swarm is nearly impossible. Although cell elongation, common for bacteria undergoing swarmer differentiation [21], improved chemotaxis at high Φ_c under moderate confinement, it had little effect under nearly two-dimensional confinement expected in the swarm. Nevertheless, it remains to be investigated whether differences in swimming behavior caused by cell differentiation in a swarm [61], such as lower tumbling bias [62], might improve their tracking of gradients [63, 64]. Furthermore, additional cohesive interactions [43] or other collective modes of motility, such as twitching [65, 66], might also affect the chemotactic ability of bacteria in the swarm.

Materials and methods

Strains and cell culture

Escherichia coli st. W3110 (RpoS+), *flu*+ or Δ*flu*, were grown at 34 ^{o}C in Tryptone Broth (TB) from a 100 fold dilution of overnight culture to an optical density at 600 nm $OD_{600} = 0.7$. Where applicable, the culture was supplemented with 0.01 % cephalexin one division time (one hour) before harvesting the cells. Cells were washed thrice and resuspended in motility buffer (10 mM KPO_4, 0.1 mM EDTA, 67 mM NaCl, pH 7) supplemented with 55 mM glucose as energy source, cooled to 4 ^{o}C for 20 min to reduce metabolic activity and then concentrated by centrifugation ($1.5\,10^3$ g, 7 min) to a final cell density of order $\Phi_c \sim 20\,\%$ ($OD_{600} \sim 100$). Series of dilutions were then performed in motility buffer, so that the amount of glucose per cell remains constant (~ 0.5 mM/OD).

Microfabrication

Molds and PDMS devices were fabricated using standard photolithography and microfabrication techniques as detailed in SI text. The fabricated devices were filled with sterile DI water for short term storage, to retain their hydrophilic properties.

Chemotaxis assay

The assay was described previously in details [48]. Reservoirs were filled with cell suspensions of the same volume fraction supplemented with either 0 or 200 μM α-methyl-D,L-aspartic acid (MeAsp). The connecting channel was 2 mm long, 1 mm wide. Bacterial motion in the middle of the channel was recorded thrice, at one hour interval, at mid-height, in phase contrast microscopy at 10$\times$ magnification, using a Mikrotron 4CXP camera (1 px = 1.4 μm, field of view $A_0 = 512 \times 512$ px^2, 1 ms exposure) running at 100 frames/s (fps).

Gradient calibration

For gradient calibration experiments, the suspensions - at various cell densities - in the second reservoir were supplemented with 100 μM fluorescein as well as attractant. The gradient was measured in wide-field fluorescence microscopy (excitation filter 470/40, emission 525/50) at 10$\times$ magnification. Images were recorded using an Andor Zyla 4.2 sCMOS camera in the middle of the channel and in the attractant reservoir, the former being divided by the latter to correct for inhomogeneous illumination.

Fourier image analysis

The movies were analyzed using three different algorithms. Differential dynamic microscopy (DDM) [45] computes differential image correlation functions (DICF), which were fitted to extract the average swimming speed of the population of cells v_0 as well as the fraction of swimming cells α. The shortcomings due to the breakdown of two assumptions of [45] – even distributions of swimming directions and round cell images – were accounted for via calibrations (SI text and SI Fig. S6). Phase differential microscopy (ΦDM) [48] determined the population averaged drift velocity of the population of cells v_d. The chemotactic velocity, corrected for the fraction of non swimmers, is then $v_{ch} = v_d/\alpha$. The map of the local velocity field was also obtained by using a local ΦDM algorithm described in details in SI text. This image velocimetry technique estimated the velocity of a group of few cells located within a region 5 μm in diameter around a position $\mathbf{r} = (x, y)$. For each time point t, the local velocity field $\mathbf{v}(\mathbf{r}, t)$ was thus calculated. The spatial Fourier transform of the velocity field $\tilde{\mathbf{v}}(\mathbf{q}, t) = \iint d\mathbf{r}\, \mathbf{v}(\mathbf{r}, t) \exp(-i\mathbf{q}.\mathbf{r})$ then led to the flow structure factor via Eq. 1, A_0 being the area of the field of view.

In situ measurement and calibration of cell body volume fraction

The calibration procedure is detailed in SI text and SI Fig. S2. Briefly, chemotaxis assay samples without a chemoattractant gradient were filled with suspensions of known OD_{600}. The maximum of the suspension's structure factor $a_1^{max}/\langle I \rangle^2$, extracted from the DICF, was a simple function of OD_{600} for each bacterial length and channel height. The relation between OD_{600} and cell body volume fraction Φ_c was evaluated by measuring the cell number density of suspensions of known OD_{600} by cell counting in flow cytometry (BD Fortessa) and the average cell length

by optical microscopy. In all experiments, $a_1^{max}/\langle I \rangle^2$ obtained from DDM then yielded the local Φ_c.

Simulations

Agent-based simulations of the rod-like chemotactic particles were performed in two dimensions with periodic boundary conditions. Rod-like particles – length L, width e – were self-propelled in an overdamped fluid at constant propulsion force and interacted by exerting forces and torques on each other in the form of a Hertzian repulsion $\mathbf{F}_{ij}^{\mathrm{el}}$ and a friction $\mathbf{F}_{ij}^{\mathrm{fr}}$. Their free running swimming speed was chosen randomly in a Gaussian distribution of mean v_0 and variance dv_0. The hydrodynamic interactions between particles were neglected, althouh $\mathbf{F}^{\mathrm{fr}}$, which was absent in previous works [15–17], could be interpreted as the result of shear in the thin layer of viscous fluid between two bacteria with different velocities, thus accounting for short range hydrodynamic interactions. The particles can be in two states, either running or tumbling. During tumbles, self-propulsion was turned off and a random torque made the particle turn, with an average magnitude chosen to match literature reported turning angle distributions [67]. The state of each particle was determined by an internal chemotaxis system evolving according to the ligand concentration experienced by the cells, first formulated in [56]. The only difference with [56] was the instantaneous tumble probability, which was set directly using the concentration of phosphorylated CheY (CheY-P), disregarding the existence of multiple motors.

The set of equations governing the position and orientation of the rods, detailed in SI text, was solved by Euler integration. Parameter values are given in SI Table S2.

Acknowledgements

The authors thank Pr. Stolz, Koch and Volz for access to the microfabrication facility and Dr. L. Laganenka for providing the Δflu mutant. This work was supported by grant 294761-MicRobE from the European Research Council.

References

[1] Dombrowski C, Cisneros L, Chatkaew S, Goldstein RE, Kessler JO (2004) Self-concentration and large-scale coherence in bacterial dynamics. *Physical Review Letters* 93(9):098103.

[2] Sokolov A, Aranson IS, Kessler JO, Goldstein RE (2007) Concentration dependence of the collective dynamics of swimming bacteria. *Physical Review Letters* 98(15):158102.

[3] Marchetti MC et al. (2013) Hydrodynamics of soft active matter. *Reviews of Modern Physics* 85(3).

[4] Sokolov A, Aranson IS (2012) Physical properties of collective motion in suspensions of bacteria. *Physical Review Letters* 109(24):248109.

[5] Dunkel J et al. (2013) Fluid dynamics of bacterial turbulence. *Physical Review Letters* 110(22):228102.

[6] Gachelin J, Rousselet A, Lindner A, Clement E (2014) Collective motion in an active suspension of escherichia coli bacteria. *New Journal of Physics* 16:025003.

[7] Lushi E, Wioland H, Goldstein RE (2014) Fluid flows created by swimming bacteria drive self-organization in confined suspensions. *Proceedings of the National Academy of Sciences of the United States of America* 111(27):9733–9738.

[8] Saintillan D, Shelley MJ (2008) Instabilities, pattern formation, and mixing in active suspensions. *Physics of Fluids* 20(12):123304.

[9] Wolgemuth CW (2008) Collective swimming and the dynamics of bacterial turbulence. *Biophysical Journal* 95(4):1564–1574.

[10] Baskaran A, Marchetti MC (2009) Statistical mechanics and hydrodynamics of bacterial suspensions. *Proceedings of the National Academy of Sciences of the United States of America* 106(37):15567–15572.

[11] Decoene A, Martin S, Maury B (2011) Microscopic modelling of active bacterial suspensions. *Mathematical Modelling of Natural Phenomena* 6(5):98–129.

[12] Subramanian G, Koch DL, Fitzgibbon SR (2011) The stability of a homogeneous suspension of chemotactic bacteria. *Physics of Fluids* 23(4):041901.

[13] Wensink HH et al. (2012) Meso-scale turbulence in living fluids. *Proceedings of the National Academy of Sciences of the United States of America* 109(36):14308–14313.

[14] Vicsek T, Czirok A, Ben-Jacob E, Cohen II, Shochet O (1995) Novel type of phase transition in a system of self-driven particles. *Phys Rev Lett* 75(6):1226–1229.

[15] Ginelli F, Peruani F, Bar M, Chate H (2010) Large-scale collective properties of self-propelled rods. *Physical Review Letters* 104(18):184502.

[16] Wensink HH, Lowen H (2012) Emergent states in dense systems of active rods: from swarming to turbulence. *Journal of Physics-Condensed Matter* 24(46):464130.

[17] Abkenar M, Marx K, Auth T, Gompper G (2013) Collective behavior of penetrable self-propelled rods in two dimensions. *Physical Review E* 88(6).

[18] Liao Q, Subramanian G, DeLisa MP, Koch DL, Wu MM (2007) Pair velocity correlations among swimming escherichia coli bacteria are determined by force-quadrupole hydrodynamic interactions. *Physics of Fluids* 19(6):061701.

[19] Drescher K, Dunkel J, Cisneros LH, Ganguly S, Goldstein RE (2011) Fluid dynamics and noise in bacterial cell-cell and cell-surface scattering. *Proceedings of the National Academy of Sciences of the United States of America* 108(27):10940–10945.

[20] Ezhilan B, Shelley MJ, Saintillan D (2013) Instabilities and nonlinear dynamics of concentrated active suspensions. *Physics of Fluids* 25(7):070607.

[21] Kearns DB (2010) A field guide to bacterial swarming motility. *Nature Reviews Microbiology* 8(9):634–644.

[22] Darnton NC, Turner L, Rojevsky S, Berg HC (2010) Dynamics of bacterial swarming. *Biophysical Journal* 98(10):2082–2090.

[23] Chen C, Liu S, Shi Xq, Chaté H, Wu Y (2017) Weak synchronization and large-scale collective oscillation in dense bacterial suspensions. *Nature* 542(7640):210 – 214.

[24] Ilkanaiv B, Kearns DB, Ariel G, Be'er A (2017) Effect of cell aspect ratio on swarming bacteria. *Physical Review Letters* 118(15):158002.

[25] Stickler D, Hughes G (1999) Ability of proteus mirabilis to swarm over urethral catheters. *Eur J Clin Microbiol Infect Dis* 18(3):206–8.

[26] Ardre M, Henry H, Douarche C, Plapp M (2015) An individual-based model for biofilm formation at liquid surfaces. *Physical Biology* 12(6):066015.

[27] Berg HC (1983) *Random Walks in Biology.* (Princeton University Press, Princeton, NJ).

[28] Colin R, Sourjik V (2017) Emergent properties of bacterial chemotaxis pathway. *Current Opinion in Microbiology* 39:24–33.

[29] Sourjik V, Wingreen NS (2012) Responding to chemical gradients: bacterial chemotaxis. *Current Opinion in Cell Biology* 24:262–268.

[30] Tu Y (2013) Quantitative modeling of bacterial chemotaxis: signal amplification and accurate adaptation. *Annu Rev Biophys* 42:337–59.

[31] Larsen SH, Reader RW, Kort EN, Tso WW, Adler J (1974) Change in direction of flagellar rotation is basis of chemotactic response in escherichia coli. *Nature* 249(5452):74–77.

[32] Stock JB, Ninfa AJ, Stock AM (1989) Protein phosphorylation and regulation of adaptive responses in bacteria. *Microbiol Rev* 53(4):450–90.

[33] Goy MF, Springer MS, Adler J (1977) Sensory transduction in escherichia coli - role of a protein methylation reaction in sensory adaptation. *Proceedings of the National Academy of Sciences of the United States of America* 74(11):4964–4968.

[34] Yi TM, Huang Y, Simon MI, Doyle J (2000) Robust perfect adaptation in bacterial chemotaxis through integral feedback control. *Proceedings of the National Academy of Sciences of the United States of America* 97(9):4649–4653.

[35] Segall JE, Block SM, Berg HC (1986) Temporal comparisons in bacterial chemotaxis. *Proceedings of the National Academy of Sciences of the United States of America* 83(23):8987–8991.

[36] Park H et al. (2010) Interdependence of behavioural variability and response to small stimuli in bacteria. *Nature* 468(7325):819–U114.

[37] Laganenka L, Colin R, Sourjik V (2016) Chemotaxis towards autoinducer 2 mediates autoaggregation in escherichia coli. *Nature Communications* 7:12984.

[38] Jani S, Seely AL, Peabody VG, Jayaraman A, Manson MD (2017) Chemotaxis to self-generated ai-2 promotes biofilm formation in escherichia coli. *Microbiology.*

[39] Budrene EO, Berg HC (1995) Dynamics of formation of symmetrical patterns by chemotactic bacteria. *Nature* 376(6535):49–53.

[40] Park S et al. (2003) Influence of topology on bacterial social interaction. *Proceedings of the National Academy of Sciences of the United States of America* 100(24):13910–13915.

[41] Saragosti J et al. (2011) Directional persistence of chemotactic bacteria in a traveling concentration wave. *Proceedings of the National Academy of Sciences of the United States of America* 108(39):16235–16240.

[42] Fu X et al. (2018) Spatial self-organization resolves conflicts between individuality and collective migration. *Nat Commun* 9(1):2177.

[43] Anyan ME et al. (2014) Type iv pili interactions promote intercellular association and moderate swarming of pseudomonas aeruginosa. *Proceedings of the National Academy of Sciences of the United States of America* 111(50):18013–18018.

[44] Lushi E, Goldstein RE, Shelley MJ (2012) Collective chemotactic dynamics in the presence of self-generated fluid flows. *Physical Review E* 86(4):040902.

[45] Wilson LG et al. (2011) Differential dynamic microscopy of bacterial motility. *Physical Review Letters* 106(1):018101.

[46] Martinez VA et al. (2012) Differential dynamic microscopy: A high-throughput method for characterizing the motility of microorganisms. *Biophysical Journal* 103(8):1637–1647.

[47] Giavazzi F, Cerbino R (2014) Digital fourier microscopy for soft matter dynamics. *Journal of Optics* 16(8):083001.

[48] Colin R, Zhang R, Wilson LG (2014) Fast, high-throughput measurement of collective behaviour in a bacterial population. *Journal of the Royal Society Interface* 11(98):0486.

[49] Kim MJ, Breuer KS (2004) Enhanced diffusion due to motile bacteria. *Physics of Fluids* 16(9):L78–L81.

[50] Dufour YS, Fu X, Hernandez-Nunez L, Emonet T (2014) Limits of feedback control in bacterial chemotaxis. *PLoS Comput Biol* 10:e1003694.

[51] Celani A, Shimizu TS, Vergassola M (2011) Molecular and functional aspects of bacterial chemotaxis. *Journal of Statistical Physics* 144:219–240.

[52] Si G, Wu T, Ouyang Q, Tu Y (2012) Pathway-based mean-field model for escherichia coli chemotaxis. *Phys Rev Lett* 109(4):048101.

[53] Schauer O et al. (2018) Motility and chemotaxis of bacteria-driven microswimmers fabricated using antigen 43-mediated biotin display. *Scientific Reports* 8:9801.

[54] Vladimirov N, Lebiedz D, Sourjik V (2010) Predicted auxiliary navigation mechanism of peritrichously flagellated chemotactic bacteria. *Plos Computational Biology* 6(3).

[55] Hu B, Tu Y (2014) Behaviors and strategies of bacterial navigation in chemical and nonchemical gradients. *PLoS Comput Biol* 10(6):e1003672.

[56] Vladimirov N, Lovdok L, Lebiedz D, Sourjik V (2008) Dependence of bacterial chemotaxis on gradient shape and adaptation rate. *Plos Computational Biology* 4(12):e1000242.

[57] Long J, Zucker S, Emonet T (2017) Feedback between motion and sensation provides non-linear boost in run-and-tumble navigation. *PLoS Computational Biology* 13(3):e1005429.

[58] Krishnamurthy D, Subramanian G (2015) Collective motion in a suspension of micro-swimmers that run-and-tumble and rotary diffuse. *Journal of Fluid Mechanics* 781:422–466.

[59] Abe T, Nakamura S, Kudo S (2017) Bioconvection induced by bacterial chemotaxis in a capillary assay. *Biochemical and Biophysical Research Communications* 483(1):277–282.

[60] Adler J (1973) Method for measuring chemotaxis and use of method to determine optimum conditions for chemotaxis by escherichia coli. *Journal of General Microbiology* 74(Jan):77–91.

[61] Turner L, Zhang RJ, Darnton NC, Berg HC (2010) Visualization of flagella during bacterial swarming. *Journal of Bacteriology* 192(13):3259–3267.

[62] Swiecicki JM, Sliusarenko O, Weibel DB (2013) From swimming to swarming: Escherichia coli cell motility in two-dimensions. *Integrative Biology* 5(12):1490–1494.

[63] Taktikos J, Stark H, Zaburdaev V (2013) How the motility pattern of bacteria affects their dispersal and chemotaxis. *PLoS ONE* 8:e81936.

[64] Waite AJ et al. (2016) Non-genetic diversity modulates population performance. *Molecular Systems Biology* 12:895.

[65] Taylor RG, Welch RD (2008) Chemotaxis as an emergent property of a swarm. *Journal of Bacteriology* 190(20):6811–6816.

[66] Oliveira NM, Fostera KR, Durham WM (2016) Single-cell twitching chemotaxis in developing biofilms. *Proceedings of the National Academy of Sciences of the United States of America* 113(23):6532–6537.

[67] Taute KM, Gude S, Tans SJ, Shimizu TS (2015) High-throughput 3d tracking of bacteria on a standard phase contrast microscope. *Nature Communication* 6:8776.

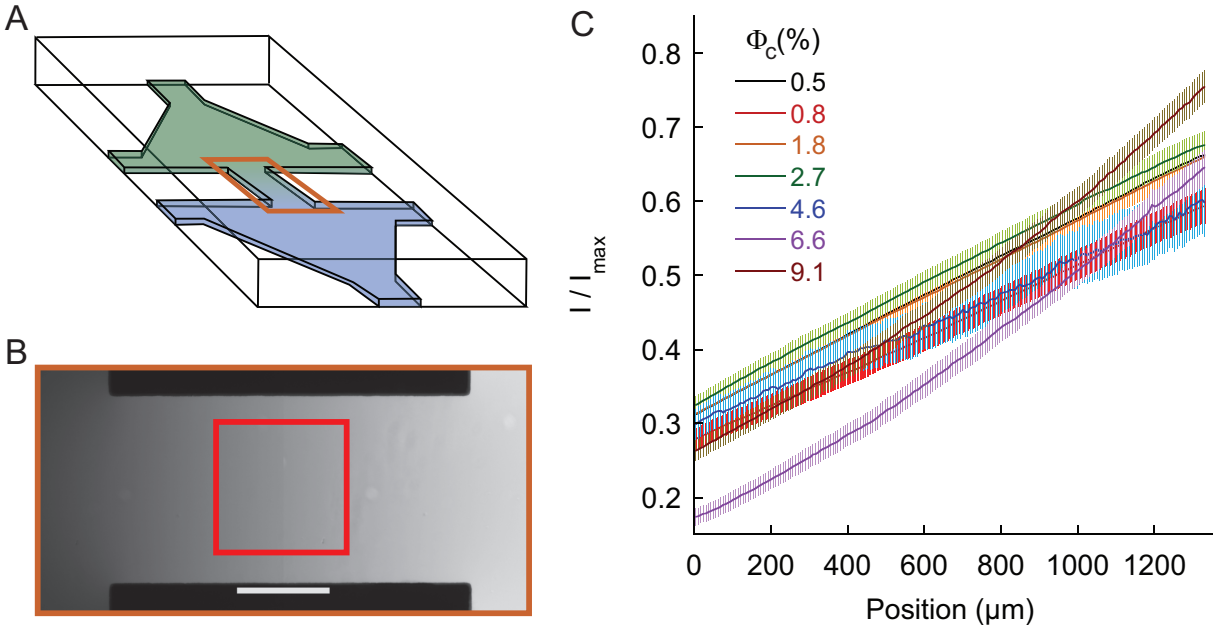

Figure 1. Microfluidic device used for chemotaxis assays. (A) Schematic representation of the device, where two reservoirs with different chemical composition are connected by a channel in which gradients of chemoattractant form. (B) Central part of the device, highlighted orange in (A), with gradient profile across the channel quantified using fluorescein. Scale bar is 500 μm. The red box indicates the location at which cellular behavior is recorded. (C) Examples of gradients, measured in the $h = 50\,\mu$m device, for cell suspensions of indicated cell densities. Error bars represent measurement error.

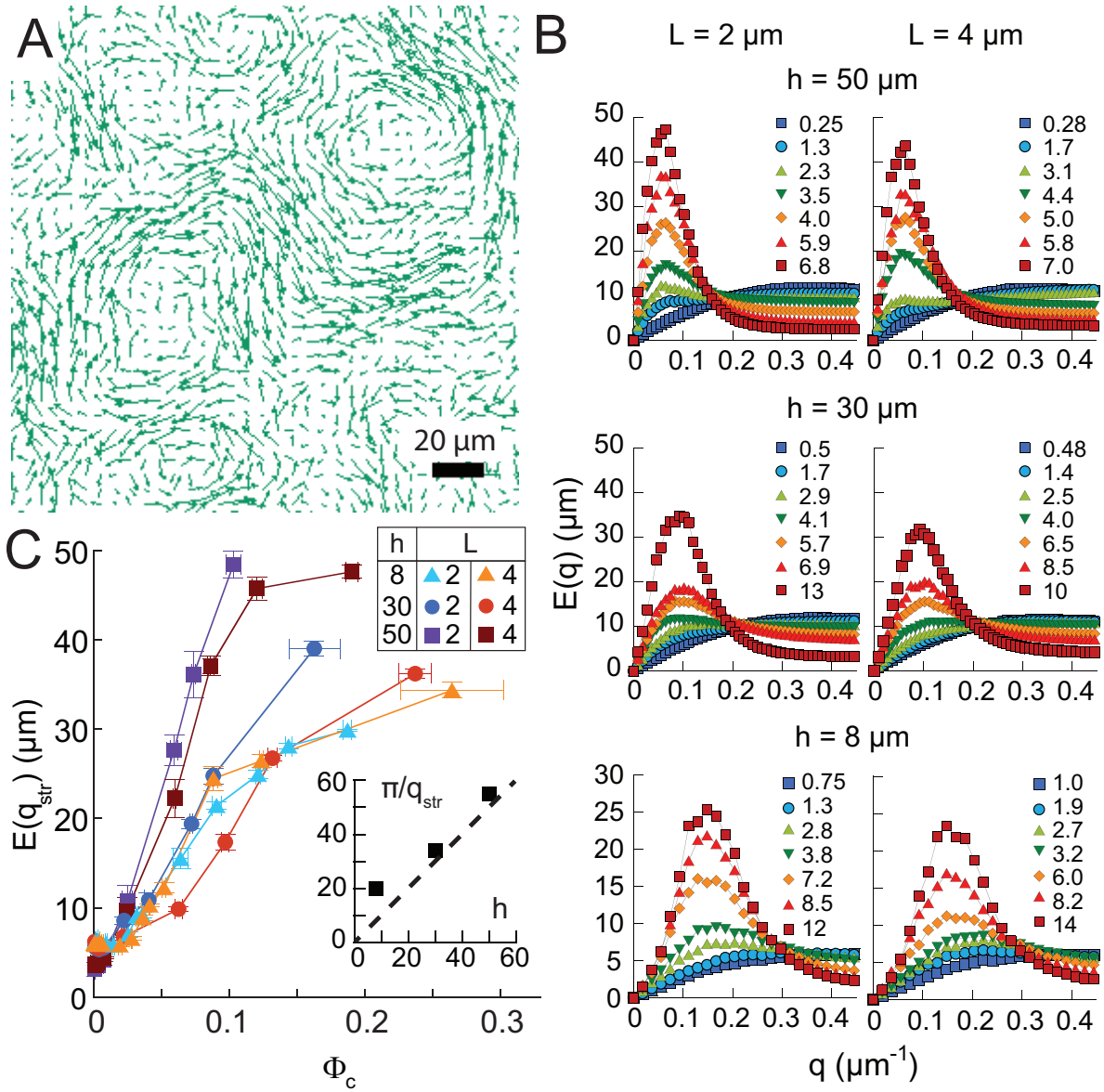

Figure 2. Collective motion in bacterial suspensions. (A) Typical snapshot of the velocity field measured in a high-density cell suspension ($\Phi_c = 8\,\%$, cell length $L = 2\,\mu$m, channel height $h = 50\,\mu$m). (B) Flow structure factor $E(q)$ for increasing cell densities at the indicated values of channel height and cell length. (C) Amplitude of the peak $E(q_{\rm str})$ as a function of cell density in the different experimental conditions. Each point is the median, and associated error bar the standard error of the mean (SEM) of 8 measurements, binned according to cell density. Inset: $\pi/q_{\rm str}$ as a function of channel height. Dashed line indicates equality.

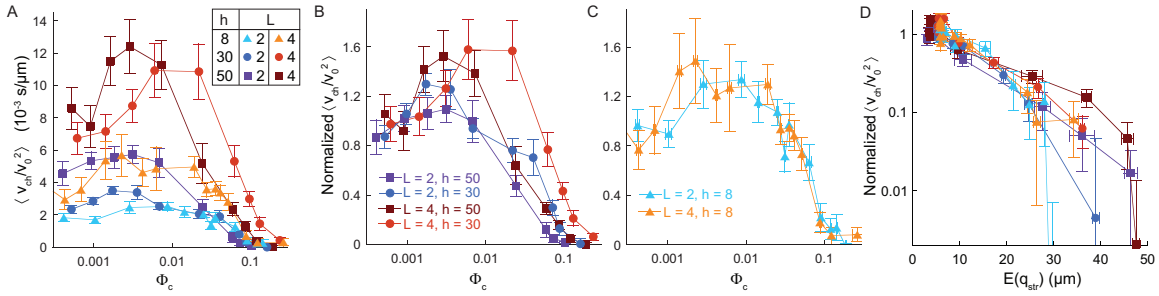

Figure 3. Effect of collective motion on the chemotactic drift. (A) Chemotactic coefficient as a function of cell density for indicated values of cell length and channel height, given in μm. (B-D) Chemotactic coefficient normalized to its low-density value as a function of cell density (B,C) or of the amplitude $E(q_{\rm str})$ of the collective motion (D). Each point represents the median of 8 experiments. Error bars represent the SEM in abscissa and the sum of the SEM and the mean measurement error in ordinate.

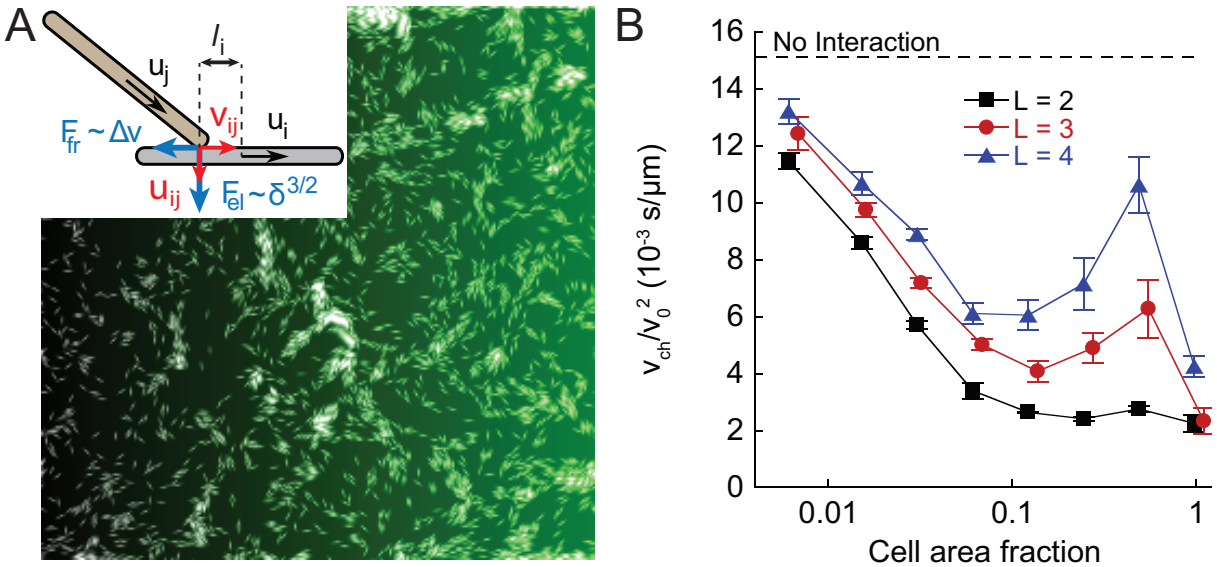

Figure 4. Numerical simulations of self-propelled interacting chemotactic rods in 2D. (A) Snapshot of a simulation output ($L = 4$, $\Phi = 0.2441$), showing collective motion of packs of cells. The green shading represents the gradient. Inset: Schematic representation of the simulated interaction between the rods, where interpenetration (δ) results in Hertzian-like repulsion ($F_{\rm el}$) and friction ($F_{\rm fr}$). (B) Chemotactic coefficient as a function of the cell area fraction, for three indicated aspect ratios (L). Error bars represent SEM on at least 3 runs.

Supporting Information (SI)

1 SI Text

1.1 Peclet number

The Peclet number compares diffusion and advection of the chemical attractant in the fluid. It is defined as $Pe = hv_f/D$, since the typical size of the flow scales with the height of the channel. Here v_f is the velocity of the fluid. It can be estimated from the difference between the high density collective velocity and the free swimming speed assumed by the cell at low density. It never exceeded $10\,\mu$m/s (SI Fig. S1). Taking the maximal $h = 50\mu$m, and considering that $D = 500\mu\text{m}^2/\text{s}$, leads to $Pe \leq 1$ for all experiments, no matter how strong the collective motion is. $Pe = 1$ indicates that distortions of the gradient are to be expected, as we observe in the case of the strongest collective motion.

1.2 Microfabrication

Molds were fabricated using standard photolithography techniques. The SU8 photoresist (Microchem ^{TM}) was spincoated on a silicon wafer for 90 s, covered with a positive mask of the device, produced using AutoCAD and printed by JD Photo Data (UK), and exposed to UV light, baked and developed according to manufacturer instructions. SU8 grade and spincoat speeds are indicated in Table S1. Poly-di-methylsiloxane (PDMS), in a 1:10 crosslinker to base ratio, was poured on the cast, degazed, baked overnight at 70° C, peeled off, cut to shape and covalently bound on isopropanol-rinsed microscopy glass slides after oxygen plasma treatment. PDMS to glass covalent bounds were allowed to form for 15 minutes at room temperature and the devices were then filled with sterile DI water for short term storage (few hours), in order to retain their hydrophilic properties.

Table S1. Spincoating parameters

height (μm)	SU8	spincoat speed (rpm)
50	2050	1500
30	2050	3000
8	2015	2500

1.3 Local image velocimetry algorithm

The image analysis algorithm is as follows, with parameter values as chosen for our analysis: In a movie of $T = 10^4$ frames of size $A_0 = L_0 \times L_0$ pixels ($L_0 = 512$), the local velocities are computed at points situated on a square lattice spaced by a distance $da = 4$ px, starting from a distance $a/2$ from the edges of the frame ($a = 32$). For this, submovies of size $a \times a$ are considered, each centered on one of the points (represented by the index k in the following) . The spatial discrete Fourier transform of the blurred time frame t in the submovie k is computed as:

$$I_k^{bl}(\mathbf{q}, t) = \iint \mathrm{d}r I_k(\mathbf{r}, t) \exp\left(-\mathbf{r}^2/l^2\right) \exp\left(-i\mathbf{q}\mathbf{r}\right) , \tag{1}$$

where $r = 0$ in the center of the submovie and $l = 3$ px is a filtering range. The size of the group of cells, for which the instantaneous velocity is computed, can thus be tuned independently of the Fourier transform parameters. Changes in pixel intensities at a distance farther than l will not contribute to the evaluation of the velocity at the point considered.

In the fashion of ΦDM [1], the phase $\delta\phi_k(\mathbf{q}, t)$ of the complex correlator $I_k^{bl}(\mathbf{q}, t+1)I_k^{bl}(\mathbf{q}, t)^*$ is computed and summed to get $\phi_k(\mathbf{q}, t) = \sum_{t'=0}^{t-1} \delta\phi_k(\mathbf{q}, t')$. This phase is fitted as a function of $\mathbf{q}$ to get the cummulated displacement $\mathbf{r}_k(t)$, $\phi_k(\mathbf{q}, t) = \mathbf{q} \cdot \mathbf{r}_k(t)$ [1]. The local instantaneous velocity $\mathbf{v}_k(t)$ is then computed by fitting:

$$\mathbf{r}_k(t') = \mathbf{r}_k(t) + \mathbf{v}_k(t)(t' - t) \tag{2}$$

on a range of $\tau = 20$ frames centered on t.

1.4 Calibration of the *in situ* measurement of cell body volume fraction

Chemotaxis assay samples were prepared as before, but without a gradient of chemotattractant, to keep the cell density as homogeneous as possible, using cell suspensions of premeasured OD_{600}. The differential image correlation functions (DCIF) $g(q, \tau) = \langle |I(\mathbf{q}, t+\tau) - I(\mathbf{q}, t)|^2 \rangle_{t, |\mathbf{q}|=q}$ were computed and fitted according to

$$g(q, \tau) = a_0(q) + a_1(q)(1 - f(q, \tau)) \,, \tag{3}$$

where $f(q, \tau)$ is the intermediate scattering function yielding the cells average swimming speed and fraction of swimmers [2]. The amplitude $a_1 \simeq g(q, +\infty) = 2\langle |I(\mathbf{q}, t)|^2 \rangle_{t, |\mathbf{q}|=q}$ is expected to scale as $a_1(q) \sim f(N_{part})\langle I \rangle^2 F(q) S(q)$, where N_{part} is the number of bacteria in the field of view, $S(q)$ is the structure factor of the bacterial fluid and $F(q)$ is a form factor describing the shape of the bacteria. As can be seen in SI Fig. S3A, $a_1(q)/\langle I \rangle^2$ has a single maximum for each OD_{600}. This maximum was found to obey the equation $a_1^{max}/\langle I \rangle^2 = 1.25 m\, \mathrm{OD}_{600}/(1 + m\, \mathrm{OD}_{600})$ (Fig. S3B), where m is a constant depending on the length of the bacteria and the height of the channel, for channel heights $h = 50\,\mu$m and $h = 30\,\mu$m. In the channel height $h = 8\,\mu$m, the data were more scattered due to the difficulty of obtaining a truly homogeneous suspension even in absence of gradient, and the equation $a_1^{max}/\langle I \rangle^2 = d_0\, m\, \mathrm{OD}_{600}/(1 + m\, \mathrm{OD}_{600})$, with d_0 also depending on cell length, was found to better describe the data (Fig. S3C). In all experiments, we then used $a_1^{max}/\langle I \rangle^2$ obtained from the DDM measurement to evaluate the local OD_{600} via the appropriate equation.

The correspondance between optical density and cell body volume fraction was determined by counting cells in suspensions of known OD_{600} flowing at 17.5 μL/min in a flow cytometer (BD Fortessa), which led to a size-dependent correspondance between cell number density (n_c) and OD_{600}. The average length L of the cells was evaluated by segmenting and fitting as ellipses phase contrast microscopy images of the cells (magnification ×40, NA 0.95) using ImageJ (Rasband, W.S., ImageJ, U. S. National Institutes of Health, Bethesda, Maryland, USA, http://imagej.nih.gov/ij/, 1997-2016.). The cell body volume fraction was then $\Phi_c = \pi r^2 L n_c$, where $r = 0.5\,\mu$m is the radius of an *E. coli* cell. The volume fraction was found to be proportional to optical density for both cell sizes, $\Phi_c = (1.78 \pm 0.03)10^{-3}\, \mathrm{OD}_{600}$ (SI Fig. S3C), yielding the local Φ_c for all experiments.

1.5 Calibrations of the swimming speed measurement

Confinement effect compensation – Classical fits of the intermediate scattering function [2] assume that the cells are swimming in 3D with equal probability in all directions. Biased swimming directions in the plane of the field of view were also shown to not affect the measurement as long as the swimming speed of the cells is the same in all directions [1] (in other words, chemotaxis, but not chemokinesis, affects the swimming speed measurement). If the distribution of swimming directions is however biased in the direction perpendicular to the field of view (z), the measured velocity *will* be systematically biased. This was notably the case when the suspension gets confined towards two dimensions, in the $h = 30$ and $8\,\mu$m channel. Analytical predictions exist for the DICF both for the 3D and 2D cases, but intermediate situations are more complex; The 3D analytical expression was thus used to extract the velocity and corrected as follows.

Since cells are partially confined in the z direction, we expect that the swimming speed v_0 measured using the formula, valid for cells swimming isotropically in three dimensions [2]:

$$f(q,\tau) = e^{-Dq^2\tau}\left(1-\alpha+\alpha\left(\frac{Z+1}{Zqv_0\tau}\right)\frac{\sin\left(Z^{-1}\tan^{-1}\lambda\right)}{\left(1+\lambda^2\right)^{Z/2}}\right), \tag{4}$$

with $\sigma_v = v_0/\sqrt{Z+1}$ and $\lambda = qv_0\tau/(Z+1)$, will be systematically biased compared to the real velocity. To evaluate this bias, the following experiment was conducted. The PDMS chips with 50 μm and 30 μm height were bound by plasma treatment facing each other and to a glass slide (SI Fig. S7*A*). Cell suspensions at $\mathrm{OD}_{600} \simeq 1$ were flown in the chamber – without a gradient created – and let to equilibrate for one hour. The motion of the bacteria was recorded successively in the two channels of different heights and the effective swimming speed v_0 was extracted using equations 3 and 4 for both channels. The ratio $v_0(30)/v_0(50)$ was found to be 1.075 ± 0.01 (SD – $N = 10$ repeats). The ratio being higher than 1 was expected since confinement makes the horizontal runs more probable and therefore increases the apparent 3D velocity. The same game played on the $h = 8\,\mu$m lead to a ratio $v_0(8)/v_0(50) = 1.14 \pm 0.02$ (SD – $N = 5$ repeats). All effective velocities obtained by 3D fitting in both devices of lower heights were divided by the corresponding factor to deduce the real swimming speed.

Effect of cell length – The formula 3 is valid only in the case of bacteria with isotropic shapes or for which the orientation of the anisotropic shape is uncorrelated with the direction of motion. This is a good approximation in the case of $2\,\mu$m long cells observed in phase contrast at 10× magnification, but not anymore for $4\,\mu$m long cells in these conditions. For anisotropic objects like rods, equation 3 becomes, in the non interacting case:

$$g(q,\tau) = a_0(q) + \langle I^2\rangle S(q)\int_0^{2\pi}\langle F(q,\theta)f(q,\theta,v\tau)\rangle \mathrm{d}\theta \tag{5}$$

were θ measures the orientation of the rods. Only when q becomes smaller than $1/a$, a being the largest size of the objects, does $F(q,\theta) \to 1$, and $g(q,\tau)$ can be fitted as in [2] (Eqs. 4 and 3) irrespective of the shape of the particles. The outcome $v_0(q)$ of the fit of the DICF is plotted for randomly chosen experiments with non-treated and elongated cells in SI Fig. S7B. For elongated cells, above $q = 0.9$ px^{-1}, the fitted v_0 decreased because of the anisotropy. We therefore used the values of v_0 in the range $q = 0.4 - 0.9$ px^{-1} to evaluate the swimming speed in the case of elongated cells, whereas $q = 0.4 - 2.0$ px^{-1} was used for the normal cells.

1.6 Simulations

Equations of motion – Agent-based simulations of the rod-like – length L, width e – chemotactic particles were performed in two dimensions. The particles were self-propelled in an overdamped fluid at constant propulsion force and we write $\mathbf{F}_{ij}^{\rm tot} = \mathbf{F}_{ij}^{\rm el} + \mathbf{F}_{ij}^{\rm fr}$ the sum of the elastic repulsion and friction generated upon contact pairwise interactions betweeen particles i and j:

$$\mathbf{F}_{ij}^{\rm el} = K_{\rm el}\, \delta_{i,j}^{3/2}\, \mathbf{u}_{ij}\,, \tag{6}$$

$$\mathbf{F}_{ij}^{\rm fr} = -K_{\rm fr}(\mathbf{v}_i - \mathbf{v}_j)\cdot \mathbf{v}_{ij}\ \mathbf{v}_{ij}\,, \tag{7}$$

with $\mathbf{u}_{ij}$ and $\mathbf{v}_{ij}$ the normalized orthogonal vectors defined in the inset of Fig. 4A of the main text, $\delta_{i,j}$ the inter-penetration depth between particle i and j and $\mathbf{v}_i$ and $\mathbf{v}_j$ their free running velocity, with a norm chosen randomly in a Gaussian distribution of mean v_0 and variance dv_0. Hydrodynamic interactions were neglected. The particles can be in two states, either running ($\Theta_i = 1$) or tumbling ($\Theta_i = 0$). The equations of motion for the position $\mathbf{r}_i$ and the orientation θ_i of particle i were:

$$\gamma^{\parallel}\frac{d\mathbf{r}_i^{\parallel}}{dt} = \gamma^{\parallel} v_i \mathbf{u}_i\, \Theta_i + \Sigma_j F_{ij}^{\rm tot,\parallel} \tag{8}$$

$$\gamma^{\perp}\frac{d\mathbf{r}_i^{\perp}}{dt} = \Sigma_j F_{ij}^{\rm tot,\perp} \tag{9}$$

$$\gamma^{r}\frac{d\theta_i}{dt} = \gamma^{r}\sqrt{D_r}\eta(t)\,(1-\Theta_i) + \mathbf{u}_i \wedge \Sigma_j l_{i,j}\mathbf{F}_{ij}^{\rm tot}\,, \tag{10}$$

where superscripts $^{\parallel}$ and $^{\perp}$ refer to the components respectively along and perpendicular to the rod axis of the annotated quantities. The translational friction coefficients read $\gamma^{\parallel} = 2\pi\eta L/\ln(L/e)$ and $\gamma^{\perp} = 2\gamma^{\parallel}$, and $\gamma^{r} = \gamma^{\parallel}L^2/6$ was the rotational friction coefficient. The particle's free swimming speed v_i was chosen randomly in a Gaussian distribution of mean v_0 and variance dv_0, and its orientation vector was $\mathbf{u}_i$. The distance between the center of mass of the particle and the contact point with particle j is $l_{i,j}$. Reorientation during tumbles was modelled using the rotational diffusion coefficient D_r and the normal Gaussian noise $\eta(t)$.

Model of the pathway – The chemotaxis pathway of *E. coli* is composed of a large superstructure (array) of coupled receptor dimers, embedded in the inner membrane of the cell, and coassembled with the cytoplasmic kinase CheA and adaptor protein CheW. The most aboundant chemoreceptors of *E. coli* are Tar (the main sensor of MeAsp) and Tsr. Chemoeffectors bind the receptors on their periplasmic domain, inducing conformational changes which cooperatively modify the autophosphorylation activity of the kinase CheA, attractants reducing kinase activity. The cooperative array organization enables to integrate and amplify signals from different receptors. The kinase then transmits its phosphates to the small diffusible molecule CheY. Phosphorylated CheY binds to the motor to induce tumbles and is dephosphorylated by CheZ. The previous reactions are subsecond so that a sudden increase in attractant concentration induces a fast drop in the probability of tumbling. Two enzymes, CheR and CheB, then respectively add and remove methyl groups to specific amino-acids of the respectively inactive and active chemoreceptors in few seconds. This slowly offsets chemoeffectors action, adapting the average kinase activity – and thus the tumbling rate – back to the intermediate value it assumes in homogeneous environments, so that subsequent stimulations can be sensed. The current methylation

level of the chemoreceptors then acts as a physical memory which represents the environment experienced by the cell a few seconds before, with which the current situation is compared.

We recall here the model of the chemotaxis pathway constructed in [3]. The chemoreceptor dimers were modeled as two-state variables interacting following a Monod-Wyman-Changeux allosteric model. The probability P_{on} of a signaling team of N_a Tar and N_s Tsr receptor dimers (and associated kinases) to be active is given by the free energy difference F between the active and inactive states as:

$$P_{on} = \frac{1}{1+e^F} \tag{11}$$

with the free energy difference:

$$F = (N_a + N_s)\,\epsilon(m) + N_a \ln\left(\frac{1+c/K_a^{\text{off}}}{1+c/K_a^{\text{on}}}\right) + N_s \ln\left(\frac{1+c/K_s^{\text{off}}}{1+c/K_s^{\text{on}}}\right), \tag{12}$$

where K_i^{off} (resp. K_i^{on}) is the binding affinity of the chemoattractant, present at concentration c, to the receptor i in its inactive (resp. active) state. The methylation dependent free energy difference $\epsilon(m)$ is linear by part, and defined as:

$$\epsilon(m) = \begin{cases} 1.0 - 0.5\,m, & 0 < m < 2 \\ -0.3\,(m-2.0), & 2 < m < 4 \\ -0.6 - 0.25\,(m-4.0), & 4 < m < 6 \\ -1.1 - 0.9\,(m-6.0), & 6 < m < 7 \\ -2.0 - (m-7.0), & 7 < m < 8 \end{cases}. \tag{13}$$

The methylation enzyme CheR methylates only inactive receptors with average rate k_R, and CheB demethylates only active ones with average rate k_B, so that the methylation level evolves according to:

$$\frac{\mathrm{d}m}{\mathrm{d}t} = k_R(1-P_{on}) - k_B P_{on} \tag{14}$$

The previous set of equation makes the fraction of active teams P_{on} evolve in time, responding and adapting to the history of concentrations experienced by the cell $c(t)$. The balance between autophosphorylation of active kinases and phosphotransfer to CheY sets the fraction of phosphorylated CheA dimers A_p as:

$$A_p = \frac{k_A\,P_{on}}{k_A\,P_{on} + k_Y}\,. \tag{15}$$

Finally, the fast phosphorylation – dephosphorylation cycle of CheY sets the fraction of phosphorylated CheY as:

$$Y_p = 19.3610\frac{k_Y\,A_p}{k_Y\,A_p + Z}\,. \tag{16}$$

If the cells are in the run state, the probability to tumble during the time step δt is given by:

$$p_t = \exp\left(-\delta t\,(Y_p)^H/\tau_t\right) \tag{17}$$

If the cell is in a tumbling state, the probability to start running again is however independent of the CheY phosphorylation level:

$$p_r = \exp\left(-\delta t/\tau_r\right) \tag{18}$$

All parameter values are given in Table S2 and are as in [3] except for N_a and N_s which were chosen to match the values expected at the OD_{600} to which our cells are grown [4].

Collective motion quantification – The time autocorrelation function of the cell velocity

$$C_v(t) = \langle \mathbf{v_i}(t+t_0) \cdot \mathbf{v_i}(t_0) \rangle_{i,t_0} \,/\, \langle \mathbf{v_i}^2(t_0) \rangle_{i,t_0} \tag{19}$$

was used to quantify intercellular interactions (SI Fig. S5A). For all aspect ratios, as the cell density increased, $C_v(t)$ decayed on an increasingly shorter time scale, indicating increased cell reorientations due to collisions and collective swirling (SI Fig. S5B). The time t_R for which $C_v(t_R) = 0.33$ was chosen to quantify the decay time, although any value in the range $0.1 - 0.4$ gave very similar results. The time t_R is expected to be determined in absence of interactions by the loss of directionality due to the tumbles, which is expected to be $t_R^{\mathrm{noInt}} = \tau(a)/(1 - \exp(-D_r\tau_r/2))$ [5], which accounts for the degree of persistance during the tumbles, and where $\tau(a) = \langle Y_p^{-H} \rangle \tau_t$ is the population averaged tumbling rate during the simulation. The time t_R was normalized by t_R^{noInt}, yielding 1 in absence of interactions and less in their presence, because of contact-induced reorientations. The chemotactic bias, normalized to its value in absence of interactions was almost a single function of the reorientation time (SI Fig. S5C) although a few points at high density and aspect ratio departed from the otherwise fairly consistent scaling.

Dual effect of physical interactions on the chemotactic drift – We noticed that the average pathway activity (measured by $a = P_{on}$) varied strongly between conditions. In absence of interactions, the chemotactic bias is expected to scale as

$$v_{ch}/v_0 = \tau_E \langle F(a) - F_0 \rangle \tag{20}$$

where τ_E is the normalized gradient strength, $F(a)$ is the free energy difference and F_0 its value in unstimulated steady state [6]. In this description, the chemoreceptor free energy shift $\langle F(a) - F_0 \rangle$ (CFES) arises from a competition between the chemoreceptor stimulation while swimming in the direction of the gradient, which tends to increase it, and adaptation which reduces it. The reorientations by rotational diffusion reduce the time spent consistantly in the direction of the gradient, thus reducing the effective strength of the stimulation while adaptation is unaffected, which results in reduced CFES and drift.

The CFES $\langle F(a) - F_0 \rangle$, normalized to its value in the non interacting case, followed a pattern similar to the chemotactic drift (SI Fig. S5D,E), although the predicted scaling was not exactly followed (SI Fig. S5F). However, $v_{ch}/v_0/\langle F(a) - F_0 \rangle$ was still dependent on the normalized reorientation time t_R/t_R^{noInt}, as a single function for all experiments (SI Fig. S5G). Hence, in our simulations, the collective motion has two effects concurring to chemotaxis reduction. First, it reduces the drop in pathway activity responsible for chemotactic drift (Eq. 20), in the same way as passive rotational diffusion as accounted for in [6]. Second, it additionally reduces the drift via active reorientations. This second effect is not accounted for by Eq. 20, derived in [6] from a description of chemotaxis at the single cell level by means of a Fokker-Planck equation. It might thus stem from currents of cell orientation – typically coming from the swirls – which breaks detailed balance of the fluxes of probability of cell orientation, and would therefore add non-equilibrium terms to the description of [6] .

Table S2. Parameters of the simulations

v_0	$20\,\mu$m.s^{-1}
dv_0	$2\,\mu$m.s^{-1}
δt	10^{-4} s
1 frame	10^{-2} s
$\nabla c/c_0$	$10^{-4}\,\mu$m^{-1}
c_0	$10^2\,\mu$M
Chemotaxis pathway	
τ_t	1 s
τ_r	0.1 s
H	10
N_a	10
N_s	10
K_a^{off}	$20\,\mu$M
K_a^{on}	3 mM
K_s^{off}	1 mM
K_s^{on}	10 mM
k_R	0.0182 s^{-1}
k_B	0.0364 s^{-1}
Z	31
k_A	5
k_Y	100
Interaction parameters	
D_r	4.17 rad^2/s
K_{el}/η	$10\,\mu$m$^{1/2}$.s^{-1}
K_{fr}/η	$0.1\,\mu$m

References

[1] Colin R, Zhang R, Wilson LG (2014) Fast, high-throughput measurement of collective behaviour in a bacterial population. *Journal of the Royal Society Interface* 11(98):0486.

[2] Wilson LG et al. (2011) Differential dynamic microscopy of bacterial motility. *Physical Review Letters* 106(1):018101.

[3] Vladimirov N, Lovdok L, Lebiedz D, Sourjik V (2008) Dependence of bacterial chemotaxis on gradient shape and adaptation rate. *Plos Computational Biology* 4(12):e1000242.

[4] Yang YL, Sourjik V (2012) Opposite responses by different chemoreceptors set a tunable preference point in escherichia coli ph taxis. *Molecular Microbiology* 86(6):1482–1489.

[5] Berg HC (1983) *Random Walks in Biology.* (Princeton University Press, Princeton, NJ).

[6] Long J, Zucker S, Emonet T (2017) Feedback between motion and sensation provides non-linear boost in run-and-tumble navigation. *PLoS Computational Biology* 13(3):e1005429.

[7] Martinez VA et al. (2012) Differential dynamic microscopy: A high-throughput method for characterizing the motility of microorganisms. *Biophysical Journal* 103(8):1637–1647.

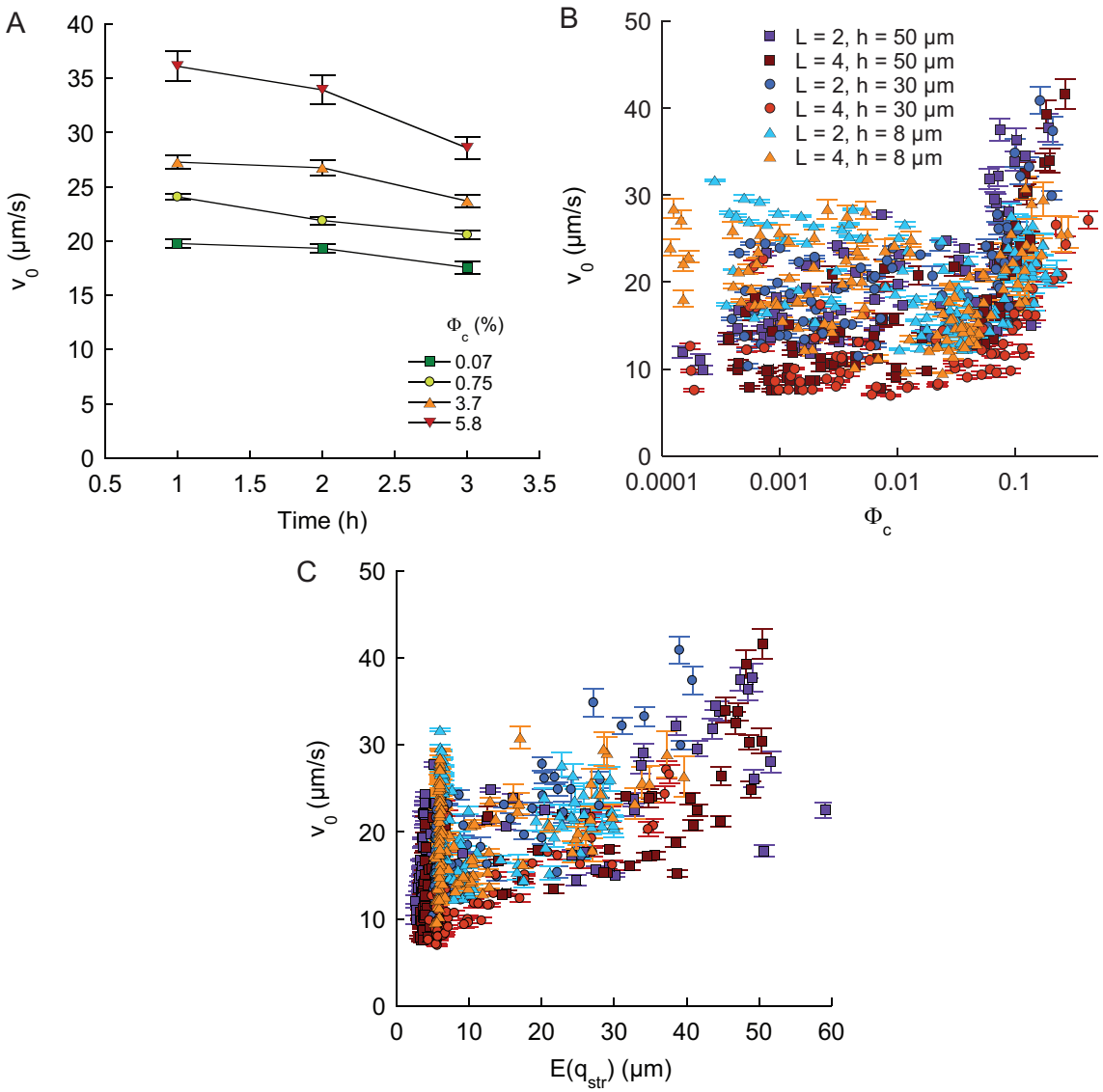

Fig. S1. (A) Examples of average swimming speed as a function of the time since sample preparation for normal cells in 50 μm high channels at indicated cell densities. The experiments were performed during the first three hours, for which swimming speed is fairly constant. (B) Average swimming speed, for all individual measurements, plotted as a function of cell body volume fraction. (C) The swimming speeds for all conditions were function of the amplitude of the collective motion, as defined in the main text, at high cell density. (A-C) Error bars represent measurement error.

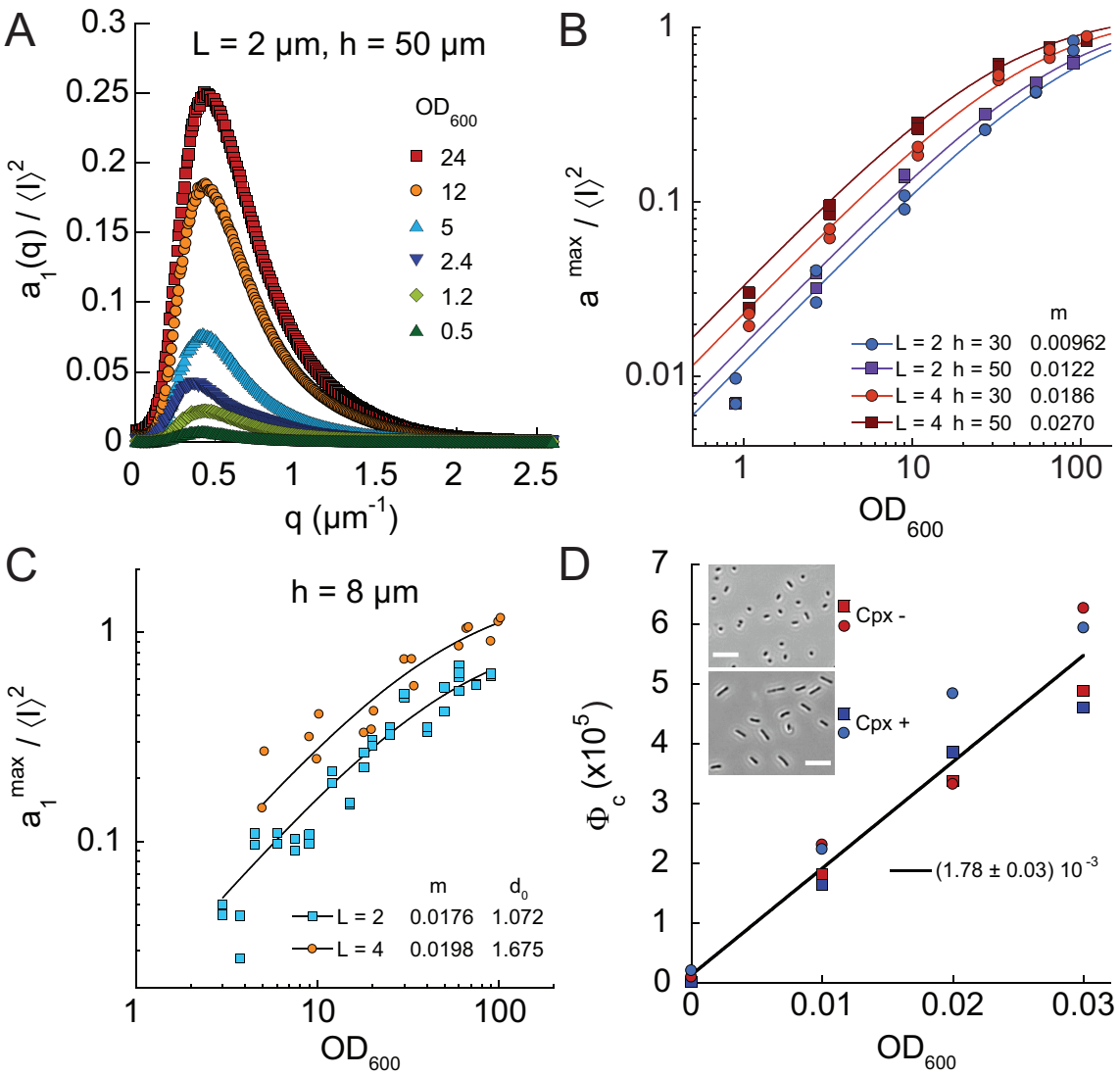

Fig. S2. *In situ* calibration of the cell body volume fraction. (A) The normalized amplitude of the differential intensity correlation function a_1/I^2, measured here in chemically homogeneous microfluidic devices, exhibits a maximum as a function of the spatial wave number q, which increases with the optical density. (B) The maximum value of a_1/I^2 can be fitted as $a_1^{max}/I^2 = 1.25\, m\, \mathrm{OD}_{600}/(1+m\, \mathrm{OD}_{600})$, with m depending on cell length L and channel height h, indicated in μm. (C) For channel height $h = 8\,\mu$m, the better adapted formula $a_1^{max}/I^2 = d_0\, m\, \mathrm{OD}_{600}/(1+m\, \mathrm{OD}_{600})$ was used. (D) The cell body volume fraction Φ_c was calibrated as a function of optical density for the single spectrophotometer used in the study, by cell counting in flow cytometry and length measurement in microscopy. The optical density was a single linear function of Φ_c, irrespective of cephalexin treatment. (Inset) Typical phase contrast images for cell length measurements, with and without cephalexin (Cpx) treatment. Scale bars are $10\,\mu$m.

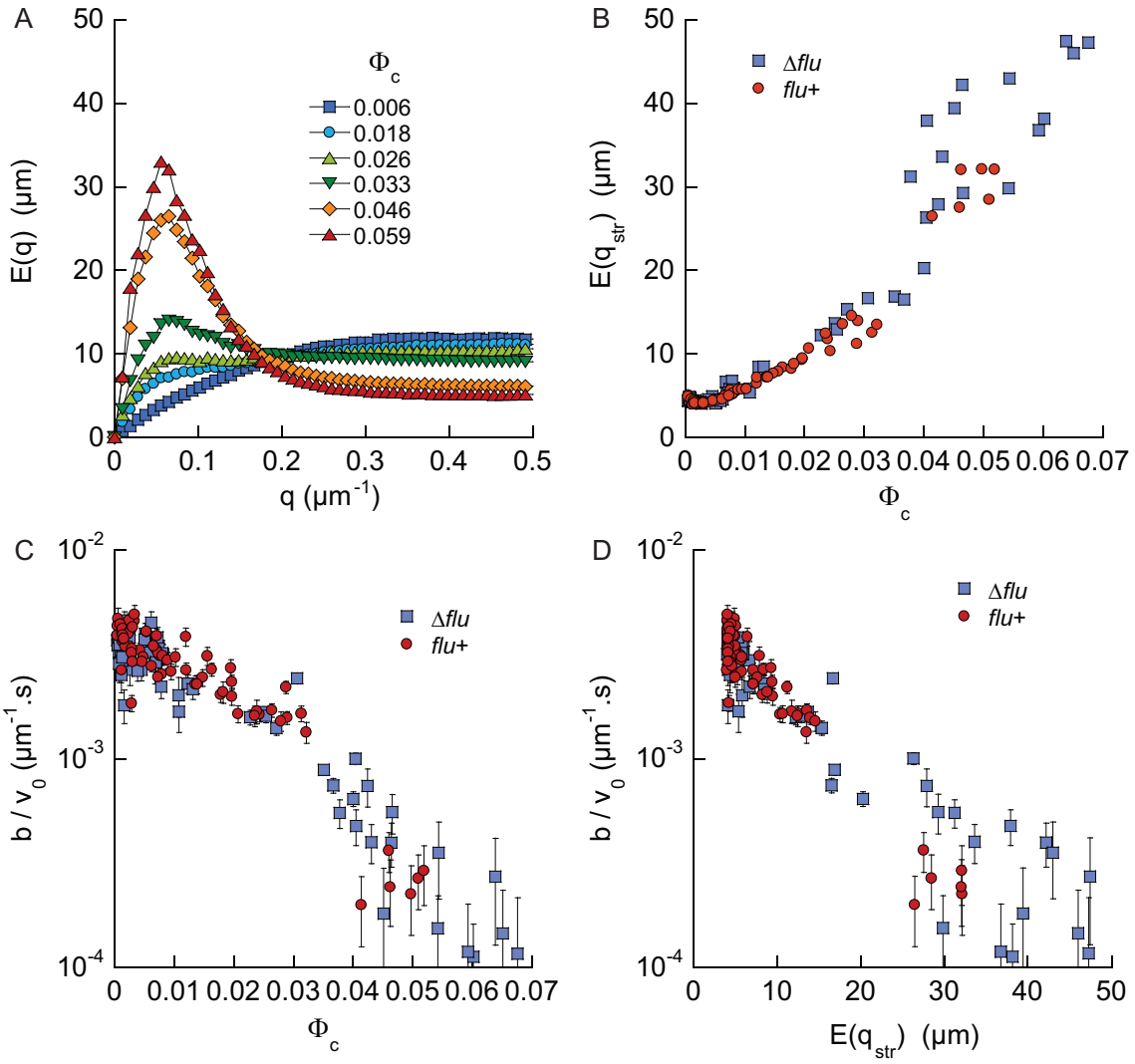

Fig. S3. Comparison of the behavior of $flu+$ and Δflu cells. (A) The spatial power spectral density E(q) measured in the 50 μm high channels exhibited a peak at $\pi/q_{str} = 50$ μm, as in the Δflu mutant, growing with cell density. (B) The maximum value of E(q) grew in exactly the same manner for both strains. (C-D) The normalized chemotactic drift had the same dependence on the cell body volume fraction (C) and on the amplitude of the collective motion $\mathrm{E(q_{str})}$ (D) in both strains.

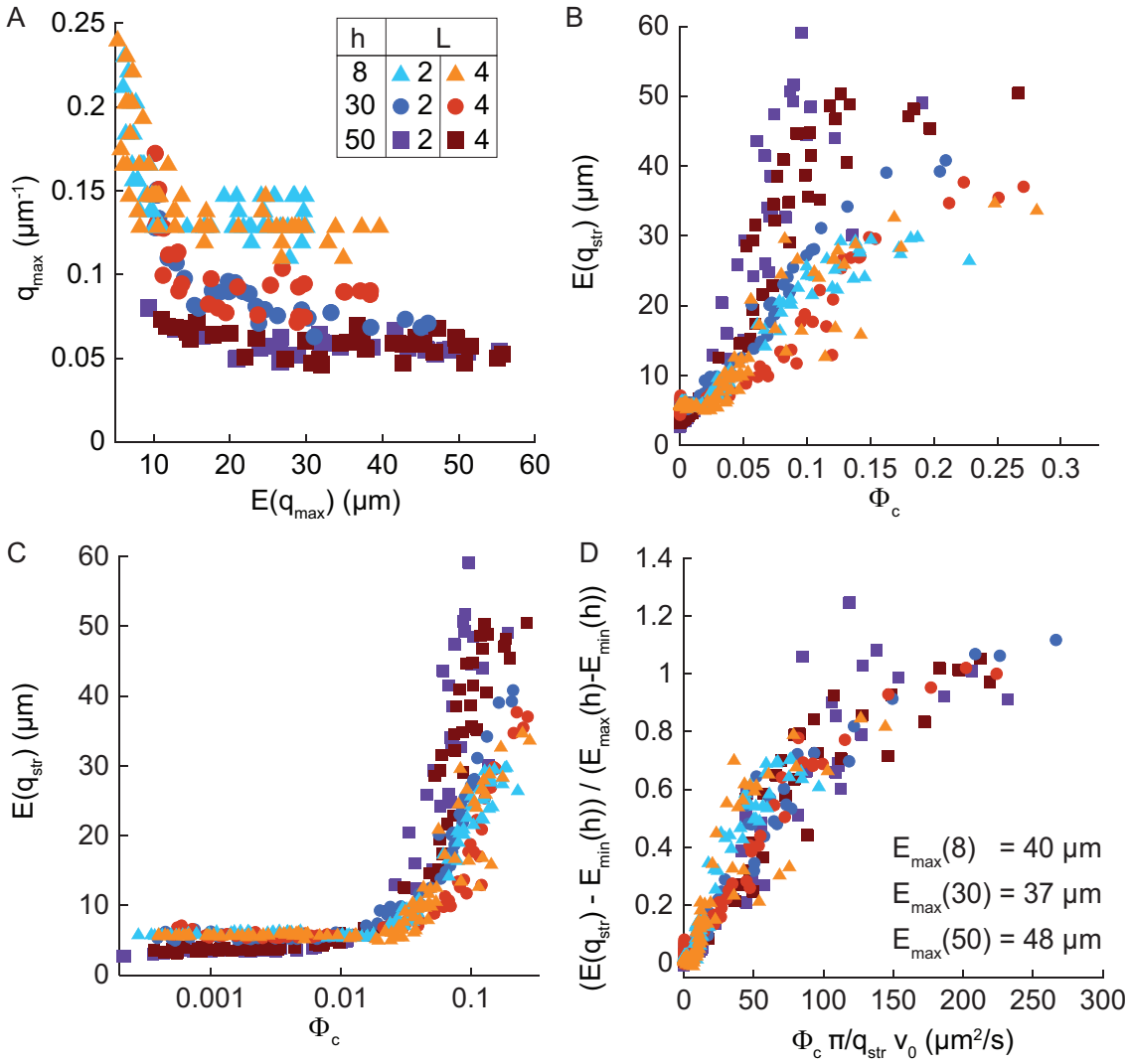

Fig. S4. Supplemental analysis of the collective motion. (A) Wave number q_{max} for which the maximum of E(q) is reached as a function of this maximum $E(q_{max})$, for all conditions. When the amplitude of the collective motion as quantified by $E(q_{max})$ is high, q_{max} reaches a plateau at q_{str}, which depends in first approximation only on the height h of the channel. Each point represents a single experiment. (B) Amplitude $E(q_{str})$ of the collective motion, measured at the plateau wave number $q_{str}(h)$, for each individual experiments, and used to draw Fig. 2C. We used $q_{str}(8\,\mu m) = 0.15\,\mu m^{-1}$, $q_{str}(30\,\mu m) = 0.093\,\mu m^{-1}$ and $q_{str}(50\,\mu m) = 0.055\,\mu m^{-1}$. (C) Same as B with Φ_c in logarithmic scale. (D) $E(q_{str})$, when corrected for its low density value $E_{\min}(q_{\mathrm{str}}(h))$ and normalized to the value at which it saturates at large density $E_{\max}(h)$, appears to be a single function of the cell body volume fraction times typical vortex size times swimming speed $(\Phi_c\,\pi/q_{\mathrm{str}}\,v_0)$.

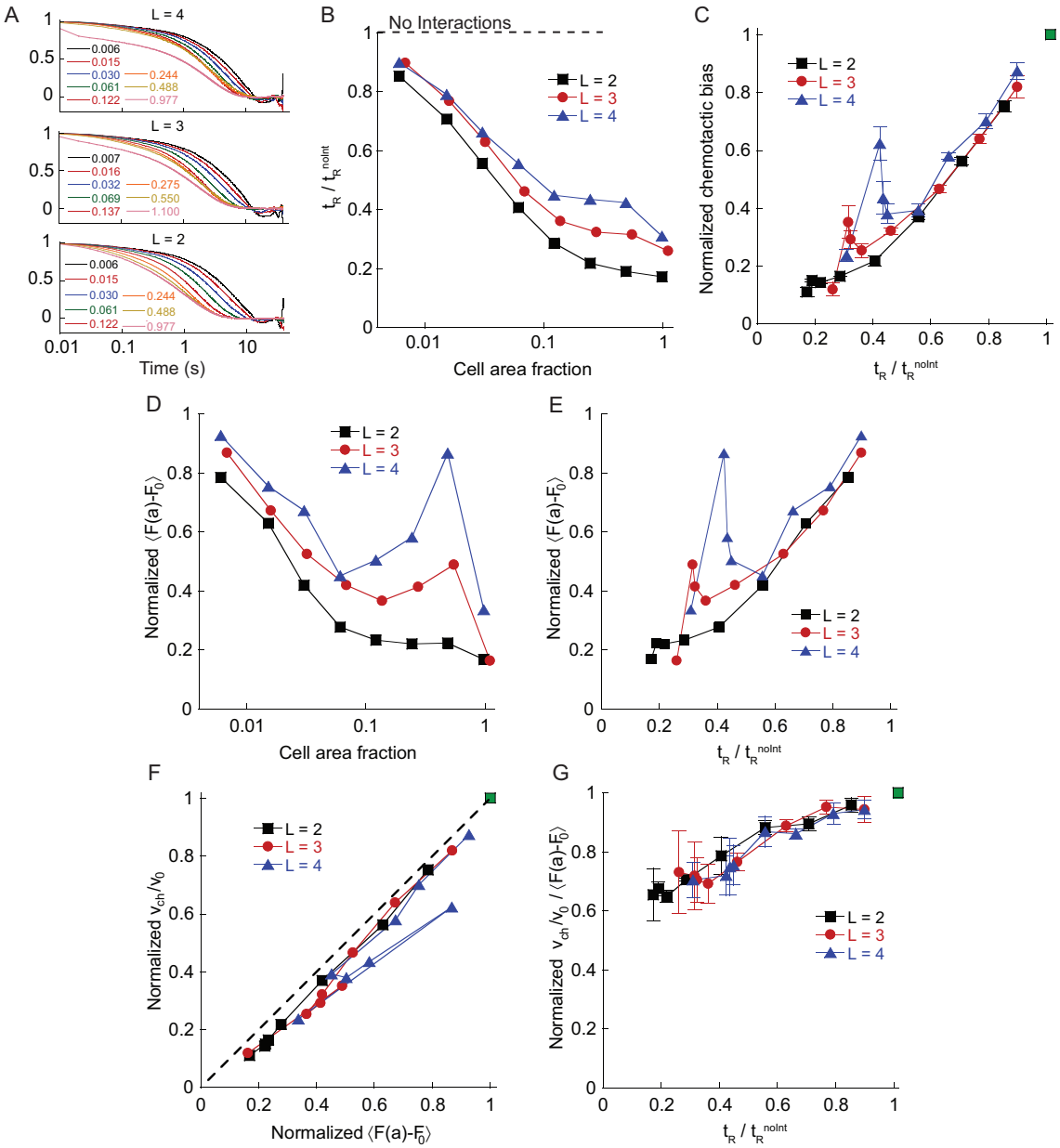

Fig. S5. Collective motion in the simulations. (A) The time autocorrelation of the cell velocity $C_v(t)$ decays more rapidly as the cell area fraction (indicated on the graphs) increases, for all aspect ratios. (B) Decay times, normalized to its expected value in absence of interaction – $t_R^{\mathrm{noInt}} = \tau(a)/(1-\exp(-D_r\tau_r/2))$, as a function of cell density. It was measured as the time for which $C_v(t_R) = 0.33$. Changing this value in the range $0.1 - 0.4$ had only minor effects on the graph. (C) The chemotactic drift, normalized to its value in abscence of interaction, as a function of the normalized decay time. The points deviating from the aspect-ratio-independent single function correspond to the peak of the chemotactic drift at high cell density for $L = 3$ and $L = 4$. (D-E) Free energy shift, normalized to its value in the non-interacting case, as a function of cell area fraction (D) or normalized decorrelation time (E). (F) Normalized chemotactic bias as a function of the normalized free energy shift. (G) The chemotactic bias normalized to the free energy shift is a single function of the normalized reorientation time.

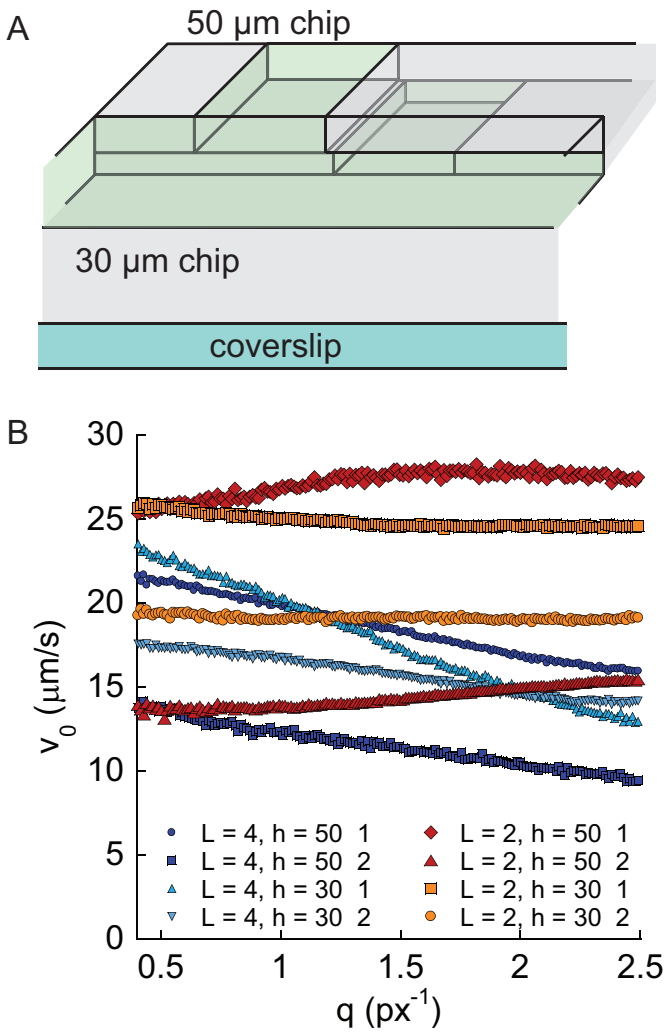

Fig. S6. Calibration of the velocity measurement by DDM. (A) Scheme of the geometry to compare DDM measurements of velocities in the 30 (or 8) μm and 50 μm devices. The two devices are facing each other and measurements can be done on the same suspension of cells in both channels. (B) Typical velocity outputs of the fit of the differential image correlation functions as a function of the wave number q, for the various experimental conditions. The effective velocity decreases for the longer cells, because of the anisotropy effect (see SI text). The slight increase for the shorter cells was attributed to tumbles in earlier studies [2, 7].